

Unconditional full vector magnetometry using spin selectivity in Nitrogen Vacancy centers in diamond

Asier Mongelos Martinez^{*,1,2}, Jason Tarunesh Francis³,
 Julia Bertero-DiTella², Geza Giedke^{3,4}, Gabriel Molina-Terriza^{2,3,4},
 Ruben Pellicer-Guridi^{†,2},

¹EHU/UPV, University of the Basque Country, Faculty of Science and Technology department of Electricity and Electroni

²Centro de Fisica de Materiales (CFM), CSIC-UPV/EHU, Paseo Manuel de Lardizabal 5,

20018 Donostia-San Sebastian, Spain,

³Donostia International Physics Center, Paseo Manuel de Lardizabal 4, 20018 Donostia-San Sebastian, Spain,

⁴IKERBASQUE, Basque Foundation for Science, Maria Diaz de Haro 3, 48013 Bilbao, Spain

* Corresponding author: amongelos003@ikasle.ehu.eus

† Corresponding author: ruben.pellicer@ehu.eus

Quantum sensors based on nitrogen vacancy (NV) centers in diamond have been a central topic in the sensing community for more than a decade. The extraordinary properties at room temperature of the spin system in diamond have made it one of the most prominent quantum platforms for the development of commercial quantum sensors. In particular, the sensitivity of the electronic spin in NV centers has made diamond-based magnetic sensors of special interest for their potential application in medical, industrial or navigation solutions. However, the use of these sensors for universal vector magnetometry was constrained by the need for previous knowledge on the field being measured to fully exploit their benefits. In this work, we show a method to perform unconditional vector magnetometry without

the need of external information on the magnetic field, based only on the spatial arrangement of the diamond and the microwave antenna combination. While previous NV-based vector magnetometry methods require partial knowledge of the magnetic field (e.g. a calibrated bias field), we exploit the possibilities of selecting particular directions of the spins in the diamond with elliptically polarized microwave fields. We prove that our method allows to estimate both magnitude and direction of external magnetic fields without further assumptions or constraints.

Magnetic field sensors are widely used in vital applications ranging from communications and navigation to medical devices such as magnetoencephalography, nuclear magnetic resonance (NMR) or magnetic marker tracking (1–4). The quest for finding high-end, yet robust and practical, magnetometers got a new impulse using quantum control of Nitrogen Vacancy (NV) centers in diamond (5). Quantum-enhanced sensors based on NV centers take advantage of their extremely sensitive electronic spin to detect external signals. Among the observables measured using NV centers are temperature (6), strain (7, 8), electric field (9–11) and most prominently magnetic field (12–16). The magnetic field dependent energy level structure of the ground state, dominated by the Zeeman-splitting, makes NV centers one of the most sensitive sensors for magnetic fields at room temperature (17, 18).

NV magnetometry relies on Electron Spin Resonance measurements (ESR) of the ground-state Zeeman splitting. A typical experimental configuration is depicted in Fig. (1 a). In bulk diamond, millions of NV centers, each oriented along one of the four crystallographic axes, enable full vector-field reconstruction (inset Fig. (1 a)) (19). In usual experiments, the ESR mixes the information of the four NV directions (as an example see Fig. (1 b), black line). In Fig. (1c) we show the limitations of the possible measurements of external magnetic fields. Existing vector-magnetometry methods solve this problem by requiring additional sensors or a bias field, in order to limit the measurements to one of the colored zones in Fig. (1 c). This imposes constraints on the hardware, limits the dynamic range, and can perturb the sample to be measured (20).

We introduce a protocol that uses MW fields with controlled elliptical polarization to selectively address NV spin states. This enables unconditional vector-field estimation—without a bias field or prior knowledge—after a single calibration of the MW field and diamond. Crucially, this removes the dynamic-range limitations imposed by the need to maintain well-separated ESR peaks, significantly

extending the usable field range of NV magnetometers. Also, while light-polarization approaches have been proposed (21–23), controlling light polarization can be slow, is easily misaligned, and more difficult to integrate in high-SNR geometries. On the other hand, we show here that the control of elliptically polarized MW fields with planar resonant antennas in diamond is an effective method to achieve spin selectivity and determine vector magnetic fields.

Theoretical background

NV magnetometry protocols probe the Zeeman effect, where an external magnetic field splits the energy of the ground state spin doublet. The large zero-field splitting ($D = 2.87$ GHz) suppresses magnetic interactions in the direction orthogonal to the NV axis up to second order perturbations (18), making NV centers highly sensitive magnetic field sensors in the direction of the NV axis. Therefore, a single NV will be mostly sensitive to the projection of the magnetic field onto the NV orientation. When interacting with a microwave field, the population of the spin states of the single NV ($|0\rangle, |+1\rangle, |-1\rangle$) can be modeled with a three-level Hamiltonian of the following form:

$$H = D S_z^2 + \gamma_e \vec{B} \cdot \vec{S} + V_{MW}(t), \quad (1)$$

$$V_{mw} = \Omega_x S_x \cos(\omega_{mw}t) + \Omega_y S_y \sin(\omega_{mw}t + \varphi), \quad (2)$$

where γ_e is the electron gyromagnetic factor, $\vec{S} = (S_x, S_y, S_z)$ is the spin-1 operator vector, and D is the zero-field splitting (typically $D = 2.87$ GHz). The general form of the microwave interaction in Eq. (2), where $\Omega_{x,y}$ are the Rabi frequencies associated with the MW field in the X, Y quadratures respectively and φ is the phase difference among the quadratures. When ω_{mw} is resonant with a transition line, the effect of the MW field is to transfer the population from the zero spin state to the ± 1 states. In this way, the Zeeman splitting can be observed directly from the frequency difference between the two peaks: $B_Z = \frac{f_1 - f_{-1}}{2\gamma_e}$, where Z is along the NV axis and $f_{\pm 1} = D \pm \gamma_e B_Z$.

To obtain the complete magnetic vector field, i.e., the projections along X and Y , we can use the other orientations of the NV centers. In a single bulk diamond crystal, NV centers lie in the four possible crystal directions defined by the C_{3v} symmetry of the NV center point defect. In particular, in this work we have used a diamond with $[1, 0, 0]$ orientation in which the four possible NV axes

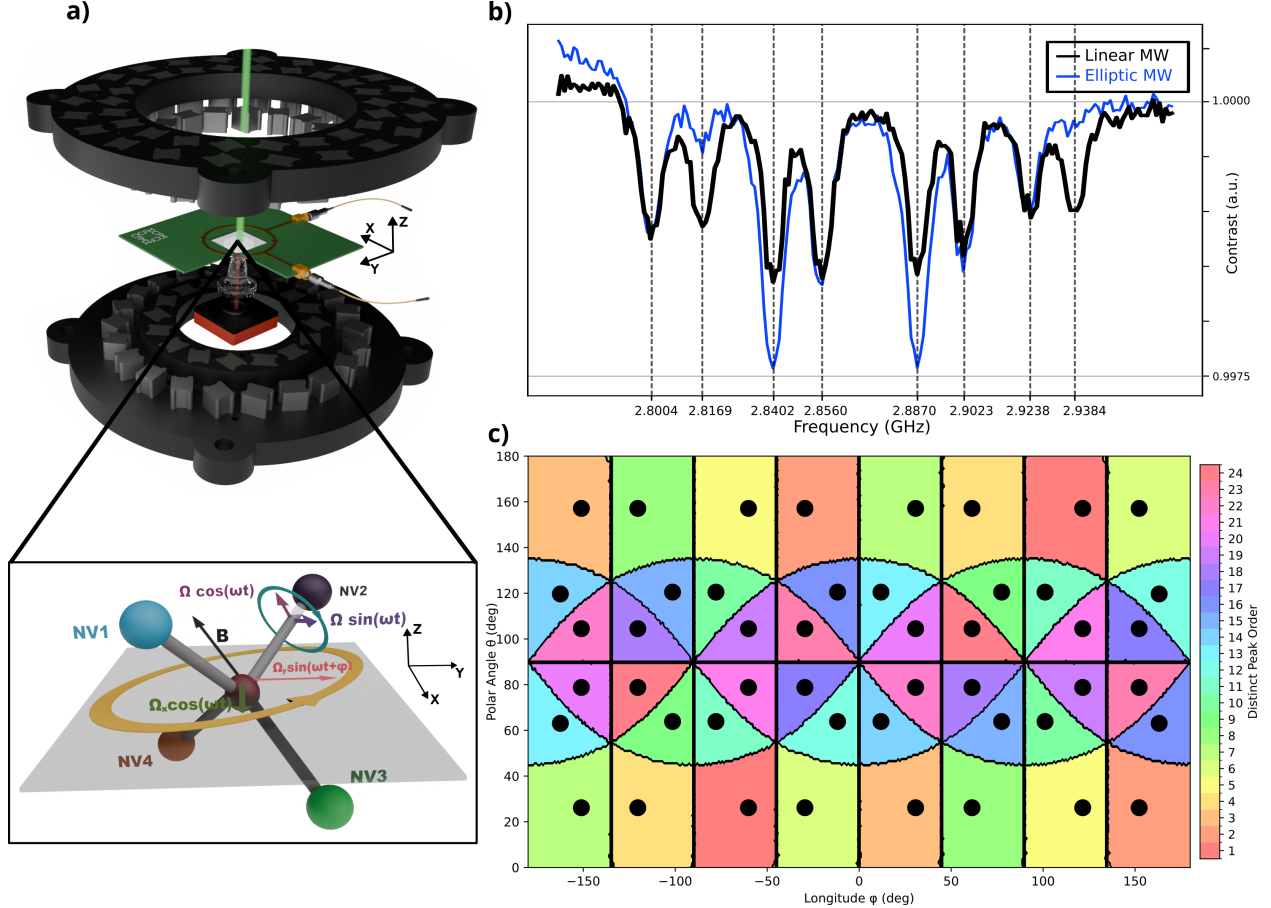


Figure 1: Schematic depiction of the protocol for bias-free vector magnetometry. *a)* Experimental setup showing the quadrature antenna with a diamond placed in the center and surrounded by Halbach arrays of permanent magnets. Laser excitation (532 nm) and fluorescence collection with a parabolic compound lens and analog detector are shown. The inset shows a schematic depiction of the spin-selective unconditional magnetometry method where elliptically polarized MW target a particular axis with circular polarization. *b)* Different peak ordering regions for magnetic field vectors in the surface of a sphere, showing the dynamic range limits of bias field magnetometry. Each color represents a distinct ordering of the directions producing the peaks in an ESR. The numbers labeling the colors correspond to each of the possible permutations of the four NV orientations ($4!$) when ordered from highest to lowest field projection, without distinguishing between positive and negative field projections. The 48 possible fields generating the ESR spectrum in *c*) are marked with dots over each colored region. *c)* Experimental measurement of an ESR with linear (black curve) and elliptically polarized (blue curve) MW showing peak attenuation from a single axis.

can be described using the following set of unit vectors (as seen in Fig. (1a)):

$$\begin{aligned}
 \hat{u}_1 &= \frac{1}{\sqrt{3}} (1, 1, 1) , \\
 \hat{u}_2 &= \frac{1}{\sqrt{3}} (-1, -1, 1) , \\
 \hat{u}_3 &= \frac{1}{\sqrt{3}} (-1, 1, 1) , \\
 \hat{u}_4 &= \frac{1}{\sqrt{3}} (1, -1, 1) .
 \end{aligned} \tag{3}$$

As a consequence, the ESR signal of a bulk diamond crystal under a magnetic field may exhibit up to eight distinct peaks corresponding to the four pairs of transition between states $|0\rangle \rightarrow |\pm 1\rangle$ along each of the four possible directions given by Eq. (3). This powerful approach allows one to perform vector magnetometry in NV centers as demonstrated by several studies (24–27). However, the unequivocal determination of a magnetic field vector depends on the association of each peak with its corresponding NV axis (15, 28, 29). Without any previous information on the magnetic field, this becomes impossible since a regular ESR measurement (Fig. (1 b), black line) is ill conditioned and does not contain the information needed to match each peak to their corresponding NV axis, resulting in the zones shown in Fig. (1 c) which limit the accessible vector magnetic fields.

In fact, due to the C_{3v} symmetry of the crystal, each ESR signal with all eight peaks discernible can lead to up to 48 possible solutions Fig. (1 c). There, all the possible magnetic field directions for a given magnetic field modulus, are presented with their azimuthal and polar angles. The configurations where the peak ordering is preserved are shown as colored areas. On the ESR example of the black line in Fig. (1 b), the possible solutions compatible with that measurement are shown in Fig. (1 c) with dots. Traditionally, this problem is solved by applying a known bias field which, even in the absence of an external field, splits the eight peaks in a known configuration (15, 18, 29). Then, much weaker external magnetic fields would shift the position of the peaks, resulting in small variations of the ESR signal which can be measured with lock-in amplifiers enabling the complete resolution of the vector magnetic field (19, 27, 30).

The bias field imposes a restriction on the available dynamic range of the NV centers as sensors, as the sum of the external and bias field should always be limited to a single colored area in Fig. (1 c). This limits the use of NV-center-based sensors in situations requiring high dynamic range. Furthermore, this strategy may affect the natural state of the samples being observed.

This can critically hinder measurements in samples experiencing magnetic forces or responding to a different range of their magnetic hysteresis, such as in studies with magnetic nanoparticles (20).

In this work we propose to use the full potential of the microwave field to selectively address different spin states corresponding to different crystal directions, as shown in Fig. (1 b), in a blue line. Here, it can be observed how different resonances behave differently for an elliptically polarized MW field. This will act as a labeling for the different peaks of the ESR spectrum. From Eqs. (1-2) if $\Omega_x = \Omega_y$ and $\varphi = 0$, i.e., a circularly polarized MW field is applied, the transfer of population only happens in $|0\rangle \rightarrow |+1\rangle$, while blocking the $|0\rangle \rightarrow |-1\rangle$ (Supplementary Text). Then, that particular transition and axis will be labeled. Tailoring these driving fields for each crystal direction, we entirely avoid the use of a bias field. This allows for the use of the full dynamic range of NV sensors and makes them competitive magnetometers. Spin selectivity using the microwave polarization and orientation has been previously proposed (25, 31–33), as well as using a single-axis configuration to demonstrate axis selectivity (23, 34, 35), for a particular scenario of a diamond cut in [111]. In this work, we exploit these properties with a fully fledged protocol that exploits all four crystal directions in a diamond cut at [100], which can be readily used for vector magnetometry.

Spin-selective vector magnetometry

To understand the protocol, note that a MW field that is circularly polarized for one direction in Eq. (4) becomes elliptically polarized for the others. Because transition selectivity requires perfectly circular MW fields, only the NV axis aligned with the designed polarization will lose one of its transition lines, while the other axes still show two peaks (with possibly different contrast). This allows us to label each pair of ESR peaks by tailoring the MW field to be circular for a chosen axis. Moreover, the handedness of the MW polarization determines the sign of the magnetic-field projection on that axis, indicated by whether the attenuated peak appears above or below the zero-field splitting at 2.87 GHz.

The technical challenge then is to produce the required MW fields for each of the NV orientations using antennas that are compatible with magnetometry measurements. A typical antenna that is well-suited for these kinds of instruments would be a resonant planar antenna. In our system, we

have used a 2-port quadrature PCB antenna capable of generating arbitrary MW signals with great homogeneity (36). These antennas can only control the polarization in the plane of the antenna. Nevertheless, as we will show below, this is enough to control the spin selectivity in the experiments. First, one starts by defining the set of right- and left-circular vector fields (\vec{r}_i, \vec{l}_i) which will address each of the $\hat{u}_i, i = 1, \dots, 4$ orientations:

$$\begin{cases} \vec{r}_i = \cos(\omega t) \vec{M}_i + \sin(\omega t) \vec{N}_i, \\ \vec{l}_i = \cos(\omega t) \vec{M}_i - \sin(\omega t) \vec{N}_i, \end{cases} \quad (4)$$

where \vec{M}_i, \vec{N}_i define 2 orthonormal vectors to the i -th axis so that $\hat{u}_i \cdot \vec{M}_i = \hat{u}_i \cdot \vec{N}_i = \vec{M}_i \cdot \vec{N}_i = 0$. If we position the antenna to lie in the XY -plane, we will then produce fields that may have a component along the NV axis:

$$\begin{cases} \vec{V}_i = (a\vec{r}_i + b\hat{u}_i), \\ \vec{T}_i = (a\vec{l}_i + b\hat{u}_i) \end{cases} . \quad (5)$$

where the coefficient a is the strength of the microwave field generating the spin rotations, and thus, proportional to the Rabi frequencies of the NV ($\Omega_{x,y}$ in Eq. (2)). The parameter b is then chosen so that the vectors \vec{V}_i and \vec{T}_i lie in the plane of the antenna, thereby producing an elliptically polarized MW field in the plane of the antenna but circularly polarised in the plane orthogonal to NV axis i (Supplementary Text). This approach is completely independent of the external magnetic field and relies only on knowledge of the diamond cut and its position in the antenna plane. In practical situations, small tilts on the crystal directions and antenna imperfections can be taken into account with a prior calibration and characterization of the system comprised of the antenna and diamond.

Results

In Fig. 2 we show experimentally how the spin selectivity is achieved. First, in Fig. (2 a) we represent the different elliptical polarizations that we achieve in the plane of the antenna and their corresponding ESR spectrum in Fig. (2 b). One can observe how each of the polarizations selectively addresses one pair of peaks, diminishing the visibility of one of them. The four polarizations were chosen using the method explained in the previous section, taking into consideration the relative directions of the NV axes with respect to the antenna plane (Supplementary Text). Moreover, in

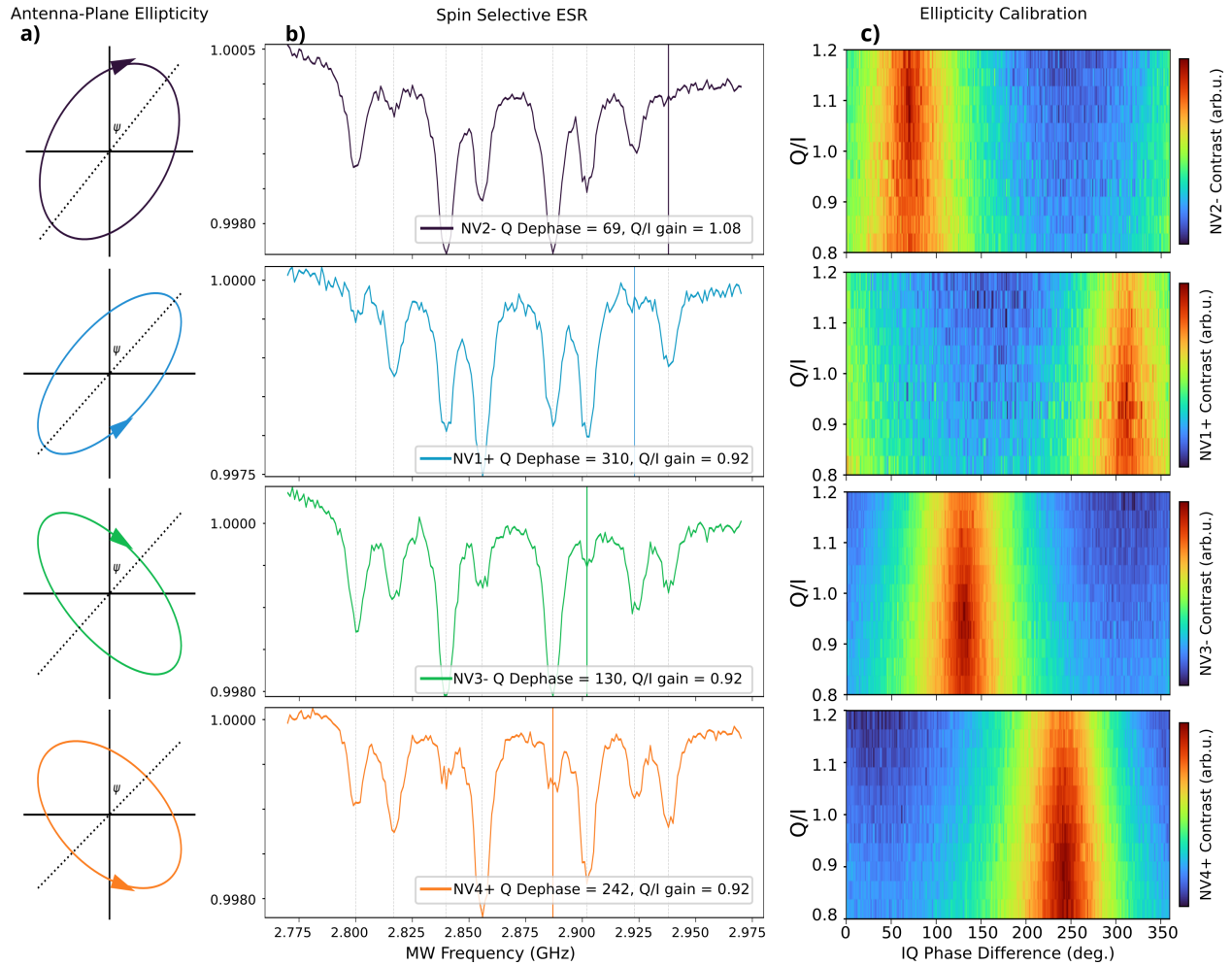


Figure 2: Experimental proof of concept, where each row shows the optimizations of MW fields to target the individual NV directions NV2 (-), NV1(+) NV3(-) and NV4(+) from top to bottom. a) MW field ellipses generated by the AWG and optimized for each crystal direction after hardware imperfections. b) ESR spectra, under driving by the corresponding calibrated MW field to the left, showing attenuation of a single NV axis enabling the identification of the peak distribution in the ESR spectrum. c) Calibration of the MW fields showing great dependency of peak attenuation to MW phase. The configurations resulting in the highest contrast correspond to the results in a) and b).

order to compensate for experimental imperfections, the visibility of the peaks was optimized by sweeping both the relative amplitude and the relative phase of the antenna feeds, denoted as the I and Q channels for MW in the X and Y directions, respectively. This is seen in Fig. (2 c). The narrow optimal regions along the phase axis reflect the extreme sensitivity of the approach to the phase of the MW (23, 34), making it possible to identify the correct phase configuration for all axes.

These results confirm the possibility of deterministically using MW field configurations to label transition lines using our proposed method. Based on the theoretical description above and assuming an experimental scenario where the diamond is tilted $\theta \sim -10^\circ$ about the Y axis and $\phi \sim 1^\circ$ around the X axis we can predict the optimal MW field configuration with a deviation up to 5° . Theoretical calculations show the optimal IQ phase differences would be 311° , 69° , 129° , 248° for NV1(+), NV2(-), NV3(-), NV4(+) respectively, which is in close agreement with the values reported in Fig. (2 b) (Supplementary Text). Remarkably, this shows the deterministic nature of the protocol where geometric characterization of the setup is sufficient to perform full vector magnetometry. This also proves the possibility to speed up calibrations using the proposed theoretical calculations and avoid wide phase and gain ratio sweeps in future measurements.

Another noteworthy effect occurs at the inner peaks (close to 2.87 GHz) where less attenuation is achieved. We attribute this effect to dipole coupling between NV centers and strain effects in high-NV-density diamond samples under low magnetic fields (37, 38). This is compensated by labeling the directions starting from the outer peaks where attenuation clearly is optimized for the corresponding axis. Once the three outer peaks are uniquely labeled, the remaining direction will correspond to the inner pair of peaks. For the inner peaks, the handedness of the elliptical polarization will determine the attenuation of each peak, reflecting the sign of the field projection.

From an independent characterization of the magnetic field we expected NV2 to have the biggest field projection followed by NV1, NV3 and NV4. Moreover, the projections of axes NV4 and NV1 were expected to be positive and those of NV3 and NV2 negative. This is also confirmed experimentally by the optimal handedness of the fields needed to attenuate the peaks with frequencies above 2.87 GHz. As shown by the ellipses in Fig. (2 a) the peaks with frequencies higher than $D = 2.87$ GHz for axis NV2 and NV3 are attenuated by a left-handed MW field. This means the peaks correspond to the $|0\rangle \rightarrow | -1 \rangle$ transition and thus the field projection in these axes is negative. Directions NV4 and NV1 use right-handed polarization owing to the positive projection of the

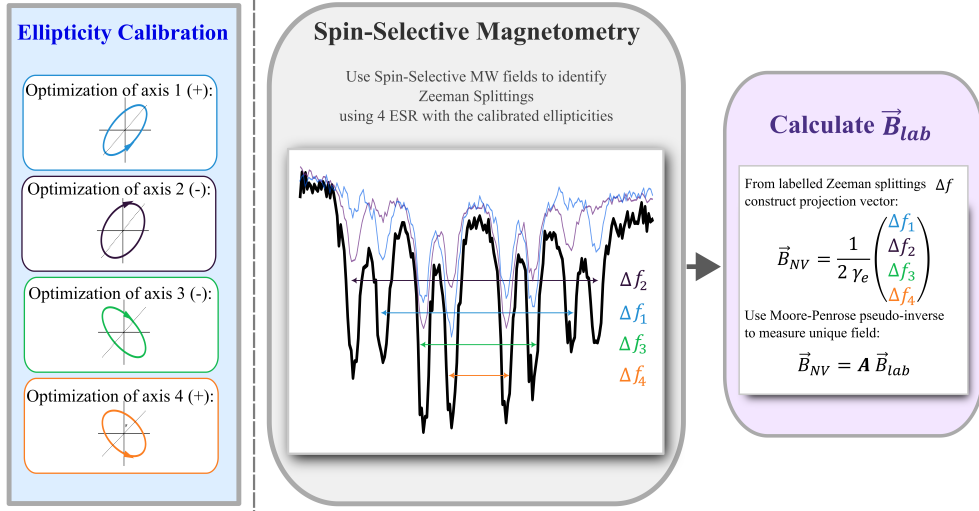


Figure 3: Unconditional Spin-Selective Vector Magnetometry. Measurement protocol based on 4 ESR measurements with pre-calibrated spin-selective MW configurations allowing exact unconditional identification of peak distribution.

field over them. The results are consistent with an independent field measurement and confirm the possibility of labeling NV axes with their corresponding transition peaks and extracting the sign of the projection of the field over them.

One can observe in Fig. 2 that although a great reduction in the visibility of the selected peaks is achieved, they are not completely attenuated, as would be expected when perfectly circular polarization is generated. This is due to the large excitation volume that is being used in this experiment ($\sim 0.5 \text{ mm}^3$). This imperfect behavior is expected due to the sharp dependence of optimal attenuation conditions to phase, and the slight inhomogeneity of ellipticity being produced in the antenna volume (see reference (36) for details). Strict peak extinction in a smaller interrogation volume using a confocal microscope setup is shown in the Supplementary Text. However, here we wanted to test the method on a realistic scenario in which large diamond volumes are used to take advantage of a higher SNR (18).

Having demonstrated that spin selectivity allows to label each one of the peaks in the ESR spectrum, we now propose a protocol to produce bias-free high-dynamic-range vector magnetometry. The protocol we propose is represented in the scheme in Fig. 3. The protocol includes a preliminary system calibration step to account for the real response of the instrument, which compensates

quadrature phase and amplitude imbalances and diamond tilts among others. This calibration can be performed under laboratory conditions and can be repeated to account for environmental factors slightly changing the antenna performance. This calibration aims to find the relative MW amplitude and phase conditions of both ports that optimize spin selectivity achieving the highest attenuation of the NV peaks. Once the right MW fields are found to address specific orientations, this information is used to define the MW antenna feed conditions and to post-process the data. The measurements can be optimized by choosing four of the configurations with their respective handedness, which provides a sufficient measurement basis. The four configurations that obtain the highest peak attenuation can be used to resolve all field projections. For any ESR spectrum the peak attenuated with each MW configuration corresponds to the axis linked to the configuration during the calibration process. When all axis transition lines and signs have been identified (step two in Fig. 3) the field projection vector can be constructed. Then knowing the axis orientations with respect to the antenna, the vector magnetic field in the laboratory-frame can be calculated using techniques such as the Moore-Penrose pseudo-inverse or best linear unbiased estimator (BLUE) of the \mathbf{A} matrix (step three in Fig. 3) (26, 27).

As a final test of the validity of our vector magnetometry protocol based on spin selectivity, we use it to discriminate two fields which would in principle be either indistinguishable in typical NV-based magnetometry or would be mutually inaccessible due to the limitations imposed by an external bias magnetic field. The two external fields in Fig. 4 belong to two different sectors in the magnetic field configuration map. These two fields produce nearly identical ESR spectra under a linear MW field excitation (black lines in the figures). However, by using the spin selectivity, we can identify that the two fields have different projections onto the NV axes, achieving the discrimination of the magnetic fields and being able to measure their vectorial components. As an example, in the figure we plot in green the differences for elliptical polarizations addressing NV3-. Once the field projections are known we solve for the magnetic field in the laboratory frame. The resultant laboratory-frame magnetic field is $\vec{B}_1 = (-11.72, -26.11, -4.80) \pm 0.06\text{G}$ which is consistent with the independent measurements of the permanent magnets used for calibration (Fig. (4 a) and black dot in Fig. (4 c)). We then perform a second measurement changing the magnetic field to have an ESR with 8 peaks but different axis ordering. We follow the protocol in Fig. 3 using the calibration above, and resolve the magnetic field $\vec{B}_2 = (24.95, -12.50, -7.77) \pm 0.06\text{G}$ (Fig. (4

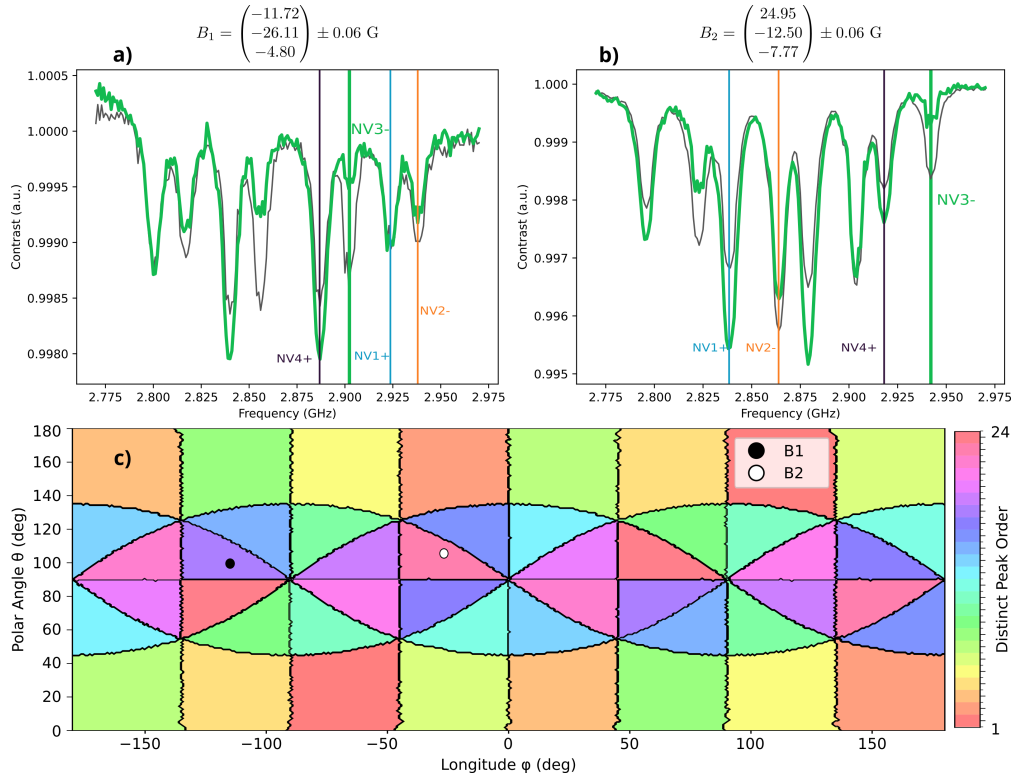


Figure 4: Unique solution of magnetic fields with similar ESR signature. *a)* *(b)* ESR measurement under magnetic field \vec{B}_1 (\vec{B}_2) with linear MW field (black line) and the optimized MW control field for NV3- (green line). *c*) Location of the resolved magnetic vectors in the configuration map of bulk NV centers, showing the calibration and protocol presented are sufficient to resolve magnetic fields generating arbitrary peak orientations with similar ESR signatures.

b) and white dot in Fig. (4 c)). This demonstrates the capability to lift the degeneracy of 48 fields producing the same spectra, and to identify a single field as the source of the signal Fig. (4c), while gaining the possibility to distinguish fields producing distinct peak ordering.

Discussion

The proposed method can resolve, without constraint, the direction of the magnetic field, which is a crucial advantage over prevailing approaches. On the one hand, this method does not need a bias field to determine the magnetic field. This not only removes the errors introduced with hardware precision limitations of the bias, but also enables measuring the magnetic field sources in their natural state. Removing the perturbation of the bias fields is particularly important, when the system under measurement or its environment does not have a linear response to magnetic fields. Similarly, the methods introducing a bias field rely on the magnitude of the measured field not being larger than the bias, constraining the dynamic range. On the other hand, other works employ additional traditional magnetometers to solve for the degeneracy of their method, which is only feasible for measurements in which the magnetic field source is far from the sensor and the magnetic field is similar in magnitude and direction on both, the NV centers and the external magnetometer.

In this work, we have aimed to prove the possibility of performing spin-selective vector magnetometry relying only on spin-control MW fields, without optimizing the measurement protocol for a particular use case. Regarding the application and versatility of the method, we acknowledge that several areas of improvement exist. A limitation of the presented method is that most of the antennas being used currently are linearly polarized and these lack the versatility to generate elliptical polarization, as needed for this method. Although, PCB-based quadrature antennas are inexpensive and readily available, tailored designs may be needed in some cases to accommodate for spatial constraints specific to certain instruments. Another factor limiting the versatility lies in the use of arbitrary waveform generator (AWG) devices, which increases the cost of any vector magnetometer based on this protocol beyond commercial feasibility. However, since the protocol only requires four pre-defined MW phase configurations for the resolution of the magnetic vector, we propose the use of standard signal generators with inexpensive programmable phase shifters

and attenuators to generate the desired relative phase and amplitude differences between channels. The use of phase shifters instead of bulky hardware also paves the way for the use of the protocol in miniaturized devices. Additionally, using less doped samples with low strain would lessen the effect of the dipolar coupling between NV centers, which equally limits the dynamic range of common NV magnetometry protocols.

Typical NV magnetometers using linear polarization of the MW fields and a magnetic bias field, only need one ESR spectrum. On the other hand, as explained, our protocol requires four different ESR spectra with different MW field configurations. We acknowledge the possibility of applying the protocol in different manners that may overcome this limitation. The presented protocol has not been designed to optimise the post-processing algorithm to select the 4 different acquisitions in the optimal SNR conditions. These processing choices can greatly affect the sensitivity of the measurements. Nonetheless, when one peak is attenuated, other peaks are enhanced. This effect partially compensate the SNR loss. In-depth analysis of optimal configurations for this protocol may depend on diverse conditions such as the crystal orientation of the NV with respect to the MW antenna. Such in-depth study is an ongoing research effort of the group and is beyond the scope of the current manuscript.

Conclusion

We present a method for unconditional spin-selective, bias-free, high-dynamic-range magnetometry with electron spin resonance of NV-center ensembles. The protocol is based only on pre-defined elliptically polarized MW fields that depend solely on the geometry of the system. This provides the means to take full advantage of the complete dynamic range provided by the Zeeman splitting of electrons in NV centers. Moreover, we measure the response of NV ensembles to MW field dephasing and show the sharp sensitivity of NV centers to phase changes on MW signals. Finally, we propose a non-optimized method to perform vector magnetometry which, upon optimization of the post-processing of measurements, could open the door to commercial applications for a high-dynamic-range sensor.

References and Notes

1. I. Lovchinsky, *et al.*, Nuclear magnetic resonance detection and spectroscopy of single proteins using quantum logic. *Science* **351** (6275), 836–841 (2016).
2. P.-B. Li, S.-Y. Gao, F.-L. Li, Quantum-information transfer with nitrogen-vacancy centers coupled to a whispering-gallery microresonator. *Physical Review A—Atomic, Molecular, and Optical Physics* **83** (5), 054306 (2011).
3. J. Vrba, S. Robinson, SQUID sensor array configurations for magnetoencephalography applications. *Superconductor Science and Technology* **15** (9), R51 (2002).
4. Z. Yu, *et al.*, Noninvasive magnetocardiography of a living rat based on a diamond quantum sensor. *Physical Review Applied* **21** (6), 064028 (2024).
5. F. A. Hahl, *et al.*, Magnetic-field-dependent stimulated emission from nitrogen-vacancy centers in diamond. *Science advances* **8** (22), eabn7192 (2022).
6. Y. Y. Hui, *et al.*, All-optical thermometry with nitrogen-vacancy centers in nanodiamond-embedded polymer films. *The Journal of Physical Chemistry C* **123** (24), 15366–15374 (2019).
7. E. MacQuarrie, T. Gosavi, N. Jungwirth, S. Bhave, G. Fuchs, Mechanical spin control of nitrogen-vacancy centers in diamond. *Physical review letters* **111** (22), 227602 (2013).
8. S. Sharma, C. Hovde, D. H. Beck, F. Alghannam, Imaging strain and electric fields in NV ensembles using stark shift measurements. *arXiv preprint arXiv:1802.08767* (2018).
9. F. Dolde, *et al.*, Electric-field sensing using single diamond spins. *Nature Physics* **7** (6), 459–463 (2011).
10. F. Dolde, *et al.*, Nanoscale detection of a single fundamental charge in ambient conditions using the NV- center in diamond. *Physical review letters* **112** (9), 097603 (2014).
11. J. Michl, *et al.*, Robust and accurate electric field sensing with solid state spin ensembles. *Nano letters* **19** (8), 4904–4910 (2019).

12. V. M. Acosta, *et al.*, Diamonds with a high density of nitrogen-vacancy centers for magnetometry applications. *Physical Review B—Condensed Matter and Materials Physics* **80** (11), 115202 (2009).
13. S. Hong, *et al.*, Nanoscale magnetometry with NV centers in diamond. *MRS bulletin* **38** (2), 155–161 (2013).
14. H. Mamin, *et al.*, Multipulse double-quantum magnetometry with near-surface nitrogen-vacancy centers. *Physical review letters* **113** (3), 030803 (2014).
15. H. Clevenson, *et al.*, Robust high-dynamic-range vector magnetometry with nitrogen-vacancy centers in diamond. *Applied Physics Letters* **112** (25) (2018).
16. K.-M. C. Fu, G. Z. Iwata, A. Wickenbrock, D. Budker, Sensitive magnetometry in challenging environments. *AVS Quantum Science* **2** (4) (2020).
17. J. F. Barry, *et al.*, Sensitive ac and dc magnetometry with nitrogen-vacancy-center ensembles in diamond. *Physical Review Applied* **22** (4), 044069 (2024).
18. J. F. Barry, *et al.*, Sensitivity optimization for NV-diamond magnetometry. *Reviews of Modern Physics* **92** (1), 015004 (2020).
19. Z. Yu, *et al.*, Experimental demonstration of a diamond quantum vector magnetometer for deep-sea applications. *National Science Review* **12** (4), nwae478 (2025).
20. G. Barrera, P. Allia, P. Tiberto, Magnetic nanoparticles in square-wave fields for breakthrough performance in hyperthermia and magnetic particle imaging. *Scientific Reports* **14** (1), 10704 (2024).
21. C. Li, F.-Z. Shi, J. Zhou, P.-F. Wang, Vector magnetometry in zero bias magnetic field using nitrogen-vacancy ensembles. *Chinese Physics B* **33** (10), 100701 (2024).
22. B. Chen, *et al.*, Calibration-free vector magnetometry using nitrogen-vacancy center in diamond integrated with optical vortex beam. *Nano Letters* **20** (11), 8267–8272 (2020).
23. H. Zheng, *et al.*, Zero-field magnetometry based on nitrogen-vacancy ensembles in diamond. *Physical Review Applied* **11** (6), 064068 (2019).

24. Z. Sun, *et al.*, Omnidirectional Diamond-Based Vector Magnetometers. *IEEE Transactions on Instrumentation and Measurement* (2025).
25. L. Childress, *et al.*, Bias-field-free operation of nitrogen-vacancy ensembles in diamond for accurate vector magnetometry. *arXiv preprint arXiv:2505.24574* (2025).
26. D. Lönard, I. C. Barbosa, S. Johansson, J. Gutsche, A. Widera, Limits of absolute vector magnetometry with NV centers in diamond. *arXiv preprint arXiv:2504.20750* (2025).
27. J. M. Schloss, J. F. Barry, M. J. Turner, R. L. Walsworth, Simultaneous broadband vector magnetometry using solid-state spins. *Physical Review Applied* **10** (3), 034044 (2018).
28. B. Zhao, *et al.*, High-sensitivity three-axis vector magnetometry using electron spin ensembles in single-crystal diamond. *IEEE Magnetics Letters* **10**, 1–4 (2019).
29. Y. Wang, *et al.*, Fully integrated quantum magnetometer based on nitrogen-vacancy centers. *Physical Review Applied* **23** (3), 034008 (2025).
30. D. Zheng, *et al.*, An integrated nitrogen-vacancy magnetometer with sub-nanotesla sensitivity for practical applications. *IEEE Sensors Journal* (2024).
31. T. Lenz, A. Wickenbrock, F. Jelezko, G. Balasubramanian, D. Budker, Magnetic sensing at zero field with a single nitrogen-vacancy center. *Quantum Science and Technology* **6** (3), 034006 (2021).
32. S. Kumar, *et al.*, High-resolution spectroscopy of a single nitrogen-vacancy defect at zero magnetic field. *Quantum Science and Technology* **8** (2), 025011 (2023).
33. J. Kölbl, M. Kasperczyk, B. Bürgler, A. Barfuss, P. Maletinsky, Determination of intrinsic effective fields and microwave polarizations by high-resolution spectroscopy of single nitrogen-vacancy center spins. *New Journal of Physics* **21** (11), 113039 (2019).
34. M. Li, *et al.*, Near-Field Sensing of Microwave Magnetic Field Phase Difference Enabled by N-V-Center Spins. *Physical Review Applied* **19** (5), 054088 (2023).
35. R. Staacke, *et al.*, Method of full polarization control of microwave fields in a scalable transparent structure for spin manipulation. *Journal of Applied Physics* **128** (19) (2020).

36. R. Pellicer-Guridi, *et al.*, Versatile quadrature antenna for precise control of large electron spin ensembles in diamond. *Advanced Quantum Technologies* **8** (3), 2400142 (2025).
37. M. Tyler, H. Zhou, L. S. Martin, N. Leitao, M. D. Lukin, Higher-order methods for Hamiltonian engineering pulse sequence design. *Physical Review A* **108** (6), 062602 (2023).
38. G. Balasubramanian, *et al.*, Nanoscale imaging magnetometry with diamond spins under ambient conditions. *Nature* **455** (7213), 648–651 (2008).

Acknowledgments

Funding: A.M.M., J.T.F., J.B., G.M.T. and R.P.G. acknowledge the support from CSIC Research Platform on Quantum Technologies Grant No. PTI-001, from IKUR Strategy under the collaboration agreement between Ikerbasque Foundation and DIPC/MPC on behalf of the Department of Education of the Basque Government, from Project No. PID2022-143268NBI00 of Ministerio de Ciencia, Innovación y Universidades, from Elkartek grant for the BetiSense project (KK-2025/00107) from the Basque Government, from Gipuzkoa Quantum (2025-QUAN-000022-01) from the Diputación de Gipuzkoa, from Proyectos de Generación de Conocimiento (PID2024-160158OA-I00) from the Spanish Agencia de Investigación Estatal and Ramón y Cajal fellowship (RYC2023-044021-I) from the Spanish Agencia de Investigación Estatal. A.M.M. also acknowledges the financial support from the Department of Education of the Basque Government through the Non-Doctoral Researcher Pre-Doctoral Formation Program, Grant No. PRE_2024_2_0180. G.G. acknowledges the grant PID2023-146694NB- I00 funded by MCIN/AEI/10.13039/501100011033.

Author contributions: A.M.M., R.P.G. and G.M.T. conceived the idea of using elliptical MW fields to target individual NV directions. A.M.M., R.P.G., J.T.F. and J.B. prepared the experimental setup and performed the measurements. A.M.M. , R.P.G. and G.M.T. analyzed the data and wrote the manuscript. A.M.M., R.P.G., G.M.T., J.T.F., J.B., G.G. discussed and interpreted the results and provided feedback for the manuscript. A.M.M. performed simulations. G.M.T. and R.P.G. provided administrative help and funding for the work.

Competing interests: There are no competing interests to declare.

Supplementary materials

Materials and Methods

Sections S1 to S4

Figs. S1 to S5

Tables S1 and S2

References (1-38)

Supplementary Materials for

Unconditional full vector magnetometry using spin selectivity in

Nitrogen Vacancy centers in diamond

Asier Mongelos Martinez*, Jason Tarunesh Francis,

Julia Bertero di Tella, Geza Giedke, Gabriel Molina-Terriza, Ruben Pellicer-Guridi[†],

* Corresponding author: amongelos003@ikasle.ehu.eus

[†] Corresponding author: ruben.pellicer@ehu.eus

This PDF file includes:

Materials and Methods

Sections S1 to S4

Figures S1 to S5

Table S1 and S2

Materials and Methods

To prove the concept experimentally the quadrature antenna with the diamond in the center is placed between two rings containing permanent magnets arranged in 8 Halbach arrays that control the external magnetic field. Laser excitation (532 nm) from a multimode fiber impinges from the upper plane of the antenna, while a parabolic compound lens immersed in index matching liquid in contact with the diamond collects the fluorescence into an analog photodetector. Filters are placed between the parabolic compound lens and the detector in order to remove the remaining excitation laser from the fluorescence. The magnetic field before the measurement is characterized to benchmark the performance of the protocol. The signals are generated at the analog outputs of an arbitrary waveform generator (AWG), amplified in identical MW amplifiers ~ 43 dB (ZHL-16W-43-S+, Mini-circuits, USA) and finally connected to the antenna ports. To compensate for differences in signal paths due to different cable length, differences in amplifier behavior or different responses of the antenna ports, the amplitude and phase of the second AWG channel (Q) is swept while maintaining the first channel (I) constant and a continuous wave ESR is performed with each configuration (18), resulting in the results in Fig. (2) of the main text. The port where the constant AWG channel is connected sets the direction of the X axis (I channel) while the out of phase channel (Q) port sets the Y axis of our laboratory frame of reference.

Supplementary Text

Effect of circular MW fields on NV centers

This section shows the explicit effect of phase difference between MW fields in the control of the electronic spin of NV centers. For this purpose, we start from the Hamiltonian described in the main text:

$$H = DS_z^2 + \gamma_e \vec{B} \cdot \vec{S} + \Omega' (S_x \cos(\omega t + \varphi_1) + S_y \sin(\omega t + \varphi_2)) . \quad (S1)$$

Moving into interaction picture with respect to ωS_z^2 and defining $\Omega = \frac{\Omega'}{\sqrt{2}}$ the resulting Hamiltonian after the rotating wave approximation becomes:

$$H' = DS_z^2 + \gamma_e B_z S_z - \omega S_z^2 + \frac{\Omega}{2} \begin{pmatrix} 0 & e^{-i\varphi_1} + e^{-i\varphi_2} & 0 \\ e^{i\varphi_1} + e^{i\varphi_2} & 0 & e^{i\varphi_1} - e^{i\varphi_2} \\ 0 & e^{-i\varphi_1} - e^{-i\varphi_2} & 0 \end{pmatrix}. \quad (\text{S2})$$

Equation (S2) shows the effect of MW handedness on electronic transitions. When $\varphi_1 = \varphi_2$, only terms coupling $|0\rangle \longleftrightarrow |+1\rangle$ will survive in the Hamiltonian generating transitions only between those states, while decoupling state $| -1 \rangle$ from the interaction. This corresponds to a right-handed circularly polarized MW field around the NV axis. On the contrary, choosing $\varphi_2 = \varphi_1 + \pi$ only the terms coupling $|0\rangle \longleftrightarrow | -1 \rangle$ will survive, decoupling state $|1\rangle$, which corresponds to a left-handed MW polarization.

Peak selective MW polarizations

The optimal microwave (MW) ellipticities to maximally attenuate the resonance lines produced by NV centers in a single crystal axis can be calculated following the procedure described in the main text. Here the explicit details and considerations of a flat and a tilted diamond in the antenna are considered. To find explicit expressions for the ellipticities, we describe the NV axis in the laboratory frame formed by taking the X and Y directions along the MW ports. As described in the main text, choosing this set of coordinates the axis orientations contain mixed terms in the XYZ directions. To ease calculations we choose a new set of coordinates X_{nv}, Y_{nv} oriented along the diamond crystal diagonals as described in equation (S3).

$$\begin{aligned} X_{nv} &= \frac{1}{\sqrt{2}} (X + Y) \\ Y_{nv} &= \frac{1}{\sqrt{2}} (Y - X) \end{aligned} \quad (\text{S3})$$

The orientations of NV directions, together with the lab frame and the newly chosen set of coordinates can be seen in figure (S1). To differentiate between laboratory frame and the diagonal frame we denote all vectors written in the former with nv . The NV axis in the X_{nv}, Y_{nv} reference frame are:

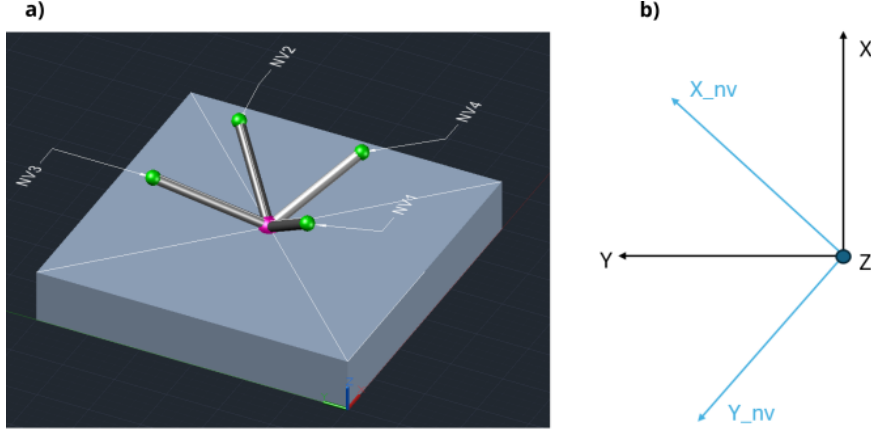


Figure S1: Schematic representation of the crystal directions and reference frames. *a*) Axis orientations in diamond. ***b*)** Chosen coordinates for NV reference frame (blue) and laboratory frame of reference (black).

$$\begin{aligned}
 \hat{u}_1^{nv} &= \left(\frac{\sqrt{2}}{\sqrt{3}}, 0, \frac{1}{\sqrt{3}} \right), \\
 \hat{u}_2^{nv} &= \left(-\frac{\sqrt{2}}{\sqrt{3}}, 0, \frac{1}{\sqrt{3}} \right), \\
 \hat{u}_3^{nv} &= \left(0, \frac{\sqrt{2}}{\sqrt{3}}, \frac{1}{\sqrt{3}} \right), \\
 \hat{u}_4^{nv} &= \left(0, -\frac{\sqrt{2}}{\sqrt{3}}, \frac{1}{\sqrt{3}} \right).
 \end{aligned} \tag{S4}$$

Using this description, we show the procedure to calculate orthogonal MW circular polarizations for each axis. The objective is to find the MW signals in the X and Y direction in the lab frame so that the effect of those polarizations is to generate a circular polarization orthogonal to a single NV axis with a modulation along that axis. If this can be done for each NV axis it will be possible to individually select each of the peaks in the ESR signal of an ensemble of NVs using only in-plane MW signals.

As described in the main text, the first step for this purpose is to find 2 orthonormal vectors to each NV axis. This is easiest to do using the XY_{nv} coordinates. In this frame of reference the NV orientations come in pairs with components in X_{nv} and Z or Y_{nv} and Z respectively, $\hat{u}_{1,2}^{nv} = (n_x, 0, n_z)$ and $\hat{u}_{3,4}^{nv} = (0, n_y, n_z)$. The orthogonal vectors for each orientation can be written as follows:

$$\begin{cases} \vec{M}_{1,2} = (0, 1, 0)_{nv} \\ \vec{N}_{1,2} = (-n_z, 0, n_x)_{nv} \end{cases} \quad \begin{cases} \vec{M}_{3,4} = (1, 0, 0)_{nv} \\ \vec{N}_{3,4} = (0, n_z, -n_y)_{nv} \end{cases} \quad (S5)$$

Following equation (S1), around each axis the right and left-handed (\vec{r}, \vec{l} respectively) circular polarizations are defined as in the main text:

$$\begin{cases} \vec{r}_i = \cos(\omega t) \vec{M}_i + \sin(\omega t) \vec{N}_i \\ \vec{l}_i = \cos(\omega t) \vec{M}_i - \sin(\omega t) \vec{N}_i \end{cases} \quad (S6)$$

However, this will not be possible to achieve with an antenna that can only generate fields in the XY plane of the laboratory, since some of these vectors orthogonal to the NV axis will have components in the Z direction. The proposed method to overcome this difficulty is to generate MW polarizations in the XY lab frame that generate the mentioned \vec{r}, \vec{l} signals over the axis together with a term parallel to the NV axis. Microwaves will only be able to rotate the spin and generate the change in fluorescence if they are orthogonal to the NV axis, while the parallel component is expected to modulate the resonance frequencies of the energy levels. This is expected to decrease the resolution of the peaks by generating line broadening, however, because of the fast oscillating microwave signals this effect is expected to average over acquisitions.

The vectors that need to be constructed can be written as:

$$\begin{cases} \vec{V}_i = (a\vec{r}_i + b\hat{u}_i) \\ \vec{T}_i = (a\vec{l}_i + b\hat{u}_i) \end{cases} . \quad (S7)$$

In this case the coefficient a will be the strength of the microwave fields generating the spin rotations, and thus, proportional to the Rabi frequencies of the NV. On the other hand, b will be a coefficient that needs to be adjusted so that the MW needed to generate these signals have no Z component in the lab frame. The vectors obtained in the NV frame are the following:

$$\begin{cases} \vec{V}_{1,2}^{nv} = (-an_z \sin(\omega t) + bn_x, a \cos(\omega t), an_x \sin(\omega t) + bn_z) \\ \vec{T}_{1,2}^{nv} = (an_z \sin(\omega t) + bn_x, a \cos(\omega t), -an_x \sin(\omega t) + bn_z) \\ \vec{V}_{3,4}^{nv} = (a \cos(\omega t), an_z \sin(\omega t) + bn_y, -an_y \sin(\omega t) + bn_z) \\ \vec{T}_{3,4}^{nv} = (a \cos(\omega t), -an_z \sin(\omega t) + bn_y, an_y \sin(\omega t) + bn_z) \end{cases} . \quad (S8)$$

Transforming this into the laboratory frame of reference the following set of vector is obtained:

$$\begin{cases} \vec{V}_{1,2} = \left(\frac{b}{\sqrt{2}}n_x - \frac{a}{\sqrt{2}}(n_z \sin(\omega t) + \cos(\omega t)), \frac{a}{\sqrt{2}}(\cos(\omega t) - n_z \sin(\omega t)) + \frac{b}{\sqrt{2}}n_x, an_x \sin(\omega t) + bn_z \right) \\ \vec{T}_{1,2} = \left(\frac{a}{\sqrt{2}}(n_z \sin(\omega t) - \cos(\omega t)) + \frac{b}{\sqrt{2}}n_x, \frac{a}{\sqrt{2}}(n_z \sin(\omega t) + \cos(\omega t)) + \frac{b}{\sqrt{2}}n_x, -an_x \sin(\omega t) + bn_z \right) \\ \vec{V}_{3,4} = \left(\frac{a}{\sqrt{2}}(\cos(\omega t) - n_z \sin(\omega t)) - \frac{b}{\sqrt{2}}n_y, \frac{a}{\sqrt{2}}(n_z \sin(\omega t) + \cos(\omega t)) + \frac{b}{\sqrt{2}}n_y, -an_y \sin(\omega t) + bn_z \right) \\ \vec{T}_{3,4} = \left(\frac{a}{\sqrt{2}}(\cos(\omega t) + n_z \sin(\omega t)) - \frac{b}{\sqrt{2}}n_y, \frac{a}{\sqrt{2}}(\cos(\omega t) - n_z \sin(\omega t)) + \frac{b}{\sqrt{2}}n_y, an_y \sin(\omega t) + bn_z \right) \end{cases} . \quad (S9)$$

If the diamond is rotated around the X or Y axes, the previous reference frame becomes tilted. To take this into account and obtain the expressions of each polarization in the laboratory reference frame, that is where the antenna works, the previously achieved vectors need to be rotated. This rotation is achieved applying the following rotation matrices:

$$R_x(\theta) = \begin{pmatrix} 1 & 0 & 0 \\ 0 & \cos(\theta) & -\sin(\theta) \\ 0 & \sin(\theta) & \cos(\theta) \end{pmatrix} \quad (S10)$$

$$R_y(\theta) = \begin{pmatrix} \cos(\theta) & 0 & \sin(\theta) \\ 0 & 1 & 0 \\ -\sin(\theta) & 0 & \cos(\theta) \end{pmatrix} . \quad (S11)$$

It will be shown that small tilts in the diamond with respect to the antenna are an effective tool to lift the degeneracy created by the symmetry of the crystal. This allows to calculate a set of microwave polarizations that will select exactly each of the peaks created by each axis direction. When the diamond is tilted the vectors calculated before become tilted, therefore any vector in the tilted diamond frame from now on is denoted with a t . To calculate the shape of each vector in the

laboratory frame the rotation matrix needs to be applied $\vec{U}_{lab} = R_x(\phi)R_y(\theta)\vec{U}^t$, where \vec{U}^t can be any of the \vec{V}_i, \vec{T}_i in equation (S9) that now become \vec{V}_i^t, \vec{T}_i^t since they are tilted. Because the antenna only creates fields in the X or Y direction of the lab frame the Z component of the vectors \vec{U}_{lab} must be canceled. This is where the component along the axis direction of magnitude b comes into play. As mentioned above, this component will not rotate the spin, but instead make a small modulation of the resonance frequency. Therefore, its magnitude can be chosen freely without affecting the effectiveness of the MW signals in selecting resonant peaks. The magnitude b that satisfies $\vec{U}_{lab} \cdot \hat{z} = 0$ needs to be found. After solving for b and plugging the solved values into the components of the vectors in the laboratory reference frame, the expressions for the signals in each port for a tilted diamond are:

$$S_i^X = a \frac{1}{\sqrt{2}n_{x,y}(\sin(\phi) + q_i \sin(\theta) \cos(\phi)) + 2n_z \cos(\theta) \cos(\phi)} \times \\ \left[s_i \sqrt{2} \sin(\omega t) (\cos(\phi) + p_i \sin(\theta) \sin(\phi)) + k_i \cos(\omega t) \left(2n_{x,y} \cos(\theta) \sin(\phi) + \sqrt{2}n_z (\sin(\theta) \sin(\phi) + \cos(\phi)) \right) \right], \quad (S12)$$

$$S_i^Y = a \frac{2n_{x,y} \sin(\theta) \cos(\omega t) + g_i \sqrt{2} \cos(\theta) (n_z \cos(\omega t) + h_i \sin(\omega t))}{\sqrt{2}n_{x,y} (\sin(\theta) \cos(\phi) + \sin(\phi)) + f_i 2n_z \cos(\theta) \cos(\phi)}. \quad (S13)$$

	$V_{1,2}$	$T_{1,2}$	$V_{3,4}$	$T_{3,4}$
s_i	-1	+1	-1	+1
p_i	-1	+1	+1	+1
q_i	-1	-1	+1	+1
g_i	+1	-1	+1	+1
h_i	+1	+1	+1	-1
f_i	-1	-1	+1	+1

Table S1: Values of the parameters in equations (S12) and (S13).

Equations (S12) and (S13) show the theoretical polarizations that would completely attenuate the peaks from a particular axis in an ideal setup. The parameter a represents the magnitude of the MW field that will be circularly polarized around the NV axis. In the experimental case the effect of hardware imperfections deviates the calibrated polarizations from these predictions. The

difference of each individual signal and their polarization is shown in figure (S2).

These general expressions show that for any diamond (cut in the [100] direction) tilted by some angle with respect to the antenna it is possible to find a set of different polarizations that will generate circular polarizations around each of the axis. Each of these polarizations would theoretically extinguish perfectly one of the resonant peaks of one axis while maintaining the 2 resonant peaks for all the other axes. Therefore, the directional resolution of the vector external magnetic field is possible using only MW fields in the XY plane.

Notice that the only difference between NV 1, 2 and 3, 4 is the sign of n_x or n_y respectively. Also, as it can be seen from equations (S12) and (S13), the components n_x and n_y always appear with a $\sin(\theta)$ or $\sin(\phi)$. Consequently, some degree of tilt is necessary to be able to choose different polarizations for each axis. Table (S2) shows the phases necessary to generate optimal circular polarizations optimal for each NV axis for a diamond tilted $\theta \sim -10^\circ$, $\phi \sim 1^\circ$. Note the theoretical predictions show similar angles to the calibrated values demonstrating the deterministic behaviour of the experiment and showing strict dependence on the geometry of the system. The difference between these theoretical values and the ones found experimentally can be explained by a different set of tilt angles in the chosen reference frame for the experimental work. Nevertheless, these values show the calibration and experimental work follow the expected theoretical behavior and could be explained with exact knowledge of the experimental setup.

These calculations are consistent with the experimental results shown in the main text. Here we present the optimal MW configurations targeting all peaks from the ESR, instead of the only 4 necessary. Note that the intrinsic tilt of the diamond in the setup together with the strict phase requirements of optimal attenuation allow to find individual MW configurations for each axis. Different effects related with hardware used to generate the optimal MW signals require a calibration of the setup. This combined with uncertainty in the exact geometry of the experiment can generate the deviations between the shown theoretical phase and gain-ratio values and the calibrated ones. However, it is worth pointing out that even if the exact experimental conditions are unknown the theoretical calculations can be used to deterministically characterize the MW fields and crystal

Ellipse	Phase difference (°)	Q/I gain
NV1 (+)	311	0.91
NV2 (+)	291	1.07
NV3 (+)	231	0.90
NV4 (+)	248	1.09
NV1 (-)	49	0.91
NV2 (-)	69	1.07
NV3 (-)	129	0.90
NV4 (-)	112	1.09

Table S2: Values of the phase between the signals in ports X and Y from equations (S12) and (S13) for the optimal polarizations of a tilted diamond.

geometry enabling spin-selective ESR measurements, and thus, perform vector magnetometry.

Flat diamond ($\theta, \phi = 0^\circ$) signals and handedness relations

When the tilt angles are null $\theta, \phi = 0$, the polarizations affecting NVs 1,2 and 3,4 respectively will become degenerate. This simplified particular case makes for a good starting point to study the different signals. When diamond is placed flat over the antenna, the expressions in equations (S12) and (S13) simplified due to the cancellation of all terms with $\sin(\theta)$ or $\sin(\phi)$. The new vectors become:

$$V_{1,2} = \begin{pmatrix} -\frac{a}{\sqrt{2}} \left(\frac{\sin(\omega t)}{n_z} + \cos(\omega t) \right) \\ -\frac{a}{\sqrt{2}} \left(\frac{\sin(\omega t)}{n_z} + \cos(\omega t) \right) \\ 0 \end{pmatrix} \quad (S14)$$

$$V_{3,4} = \begin{pmatrix} \frac{a}{\sqrt{2}} \left(\cos(\omega t) - \frac{\sin(\omega t)}{n_z} \right) \\ \frac{a}{\sqrt{2}} \left(\cos(\omega t) + \frac{\sin(\omega t)}{n_z} \right) \\ 0 \end{pmatrix} \quad (S15)$$

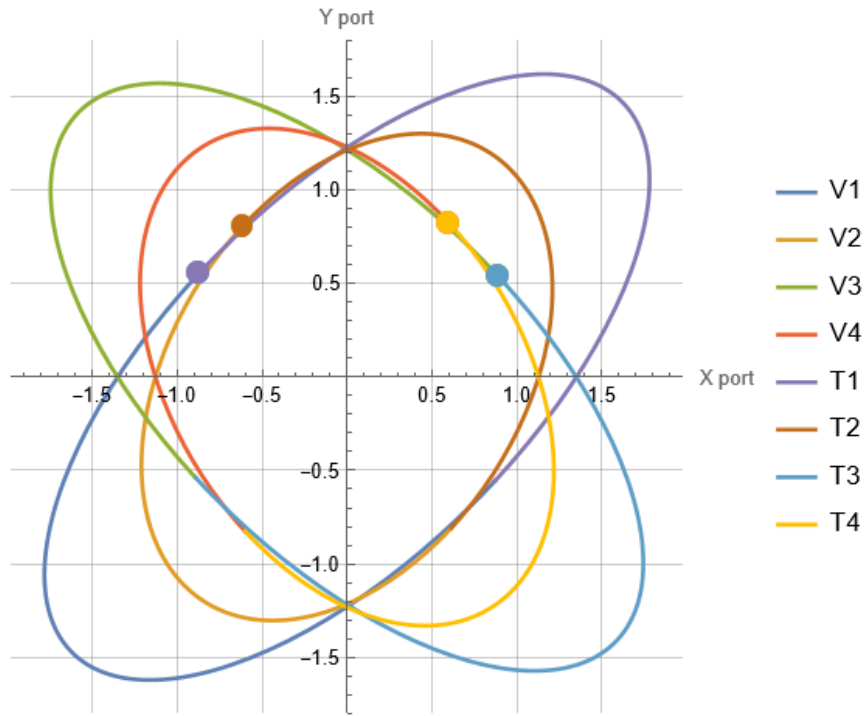


Figure S2: Theoretical optimal spin-selective MW control fields. MW field ellipses generating optimal circularly polarized control pulses over each NV axis for a diamond tilted by $\theta \sim -10^\circ$ and $\phi \sim 1^\circ$ calculated using the expressions from equations (S12) and (S13). The points indicate the starting points of the ellipses and half of their period is drawn to identify right- and left-handed polarizations.

$$T_{1,2} = \begin{pmatrix} \frac{a}{\sqrt{2}} \left(\frac{\sin(\omega t)}{n_z} - \cos(\omega t) \right) \\ \frac{a}{\sqrt{2}} \left(\frac{\sin(\omega t)}{n_z} + \cos(\omega t) \right) \\ 0 \end{pmatrix} \quad (S16)$$

$$T_{3,4} = \begin{pmatrix} \frac{a}{\sqrt{2}} \left(\cos(\omega t) + \frac{\sin(\omega t)}{n_z} \right) \\ \frac{a}{\sqrt{2}} \left(\cos(\omega t) - \frac{\sin(\omega t)}{n_z} \right) \\ 0 \end{pmatrix} \quad (S17)$$

These can be rewritten as sine waves with a fixed phase difference. Taking the signal in the X direction as the reference the previous vectors can be written as follows:

$$V_{1,2} = \begin{pmatrix} \sqrt{2}a \sin(\omega t) \\ \sqrt{2}a \sin(\omega t - \frac{\pi}{3}) \\ 0 \end{pmatrix} \quad (S18)$$

$$V_{3,4} = \begin{pmatrix} \sqrt{2}a \sin(\omega t) \\ \sqrt{2}a \sin(\omega t + \frac{4\pi}{3}) \\ 0 \end{pmatrix} \quad (S19)$$

$$T_{1,2} = \begin{pmatrix} \sqrt{2}a \sin(\omega t) \\ \sqrt{2}a \sin(\omega t + \frac{\pi}{3}) \\ 0 \end{pmatrix} \quad (S20)$$

$$T_{3,4} = \begin{pmatrix} \sqrt{2}a \sin(\omega t) \\ \sqrt{2}a \sin(\omega t + \frac{2\pi}{3}) \\ 0 \end{pmatrix} \quad (S21)$$

These expressions show the relation in phase and amplitude needed between the signal in each port of the antenna to generate the peak and axis-selective polarizations. In this non-tilted diamond scenario to target the peak corresponding to the transition $m_s = 0, 1$ NVs 1 and 2 require that the signal in the Y direction has a $-\frac{\pi}{3}$ phase and the same amplitude, while for NVs 3, 4 the dephase

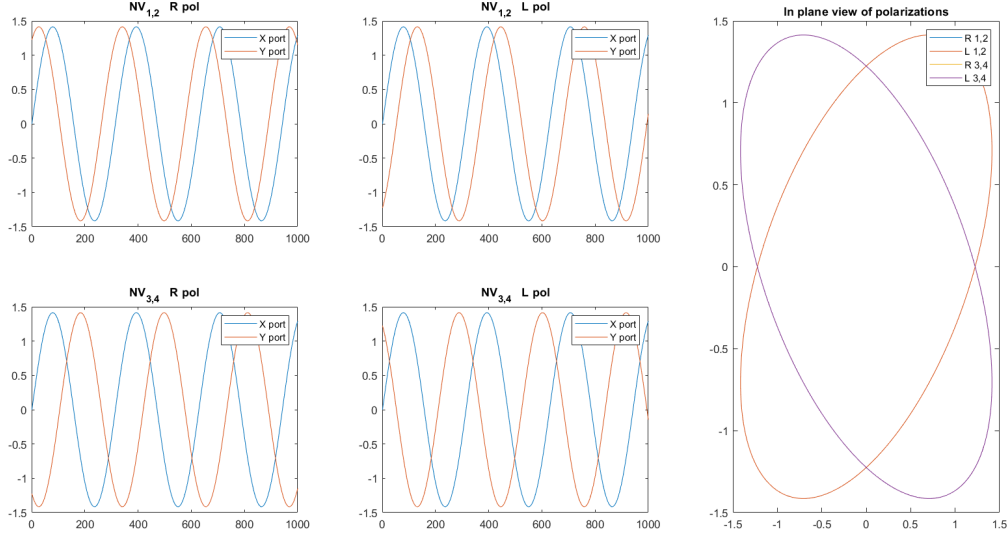


Figure S3: Optimal MW fields for flat diamond sample. Signals to select transitions peaks in ESR spectrum for the different NV orientations. Because the diamond is not tilted now the symmetry of the system makes that the peaks can only be selected by pairs. Notice the right-handed polarizations in the in-plane view are the same as the left handed, but have been covered by these when plotting.

must be of $\frac{4\pi}{3}$. To target the transitions $|0\rangle \rightarrow |-1\rangle$ NVs 1, 2 require the same amplitude in both directions but the Y direction must be out of phase by $\frac{\pi}{3}$, while for NVs 3, 4 this direction must be out of phase by $\frac{2\pi}{3}$ while maintaining the same amplitude. Notice, the power that will be inverted in rotating the spin will be a fraction $\frac{1}{\sqrt{2}}$ of the amplitude introduced in each port. These signals are visualized in Fig. S3.

Diamond flat on antenna experimental verification

In order to test the effect of diamond tilt with respect to the antenna and find complete peak attenuation, the calibration steps described in the main text were repeated using a home-made confocal microscope.

The use of the confocal microscope allowed to obtain a more precise placement of the diamond in the center of the antenna, thanks, to the higher accessibility to the sample. Besides, the small confocal volume used for excitation and fluorescence collection means the MW fields in the interrogated area are substantially more homogeneous than in the experiments shown in the main text. The results of

the calibration are shown in figure (S4). From the found optimal MW configurations the effect of the tilt can be observed. Compared to the measurement in the main text, where the diamond was tilted, peaks are attenuated by pairs. The MW configuration attenuating one peak always has almost the same effect on another peak as expected from the theoretical results for a flat diamond. This confirms the need of some tilt in the diamond to uniquely resolve the vector magnetic field with independent phase configurations. Besides, the smaller collection and excitation volume resulting in more homogeneous signals gets reflected in the optimal peak attenuation. Most peaks in these measurements get almost perfectly attenuated meaning, all NV centers in each axis are affected by the same MW fields which can be set to be completely circular. Looking at the optimal phases the slight differences in phase ($\sim 5^\circ$) can be explained by a small tilt in the diamond due to imprecise placing in the antenna, and errors in the definition of the optimal MW field due to noise in the measurement.

Phase dependence of peak attenuation

To verify the sharp dependence of peak attenuation with the phase between MW ports, we perform simulations of a MW pulse over NV centers. Starting from the Hamiltonian in equation (S2) we set a fixed value of Ω and evolve state $|0\rangle$ under the time evolution operator of a π -pulse $U_\pi = \exp\left(-iH'(\varphi)\frac{1}{2\Omega}\right)$ choosing $\omega = D + \gamma_e B$. The population of states $|0\rangle$, $|\pm 1\rangle$ are readout at the end of the pulse for different values of the phase difference between MW ports (φ). The results are shown in Fig. S5. The simulation shows the probability of a transition occurring during the π -pulse is high for a wide range of phase difference values, while in a narrow region close to perfect circular polarization the transition is prohibited resulting in peak attenuation in an ESR measurement. The theoretical results reflect the experimental results in this work, where peak attenuation is sharply dependent on MW phase difference (Fig. S5).

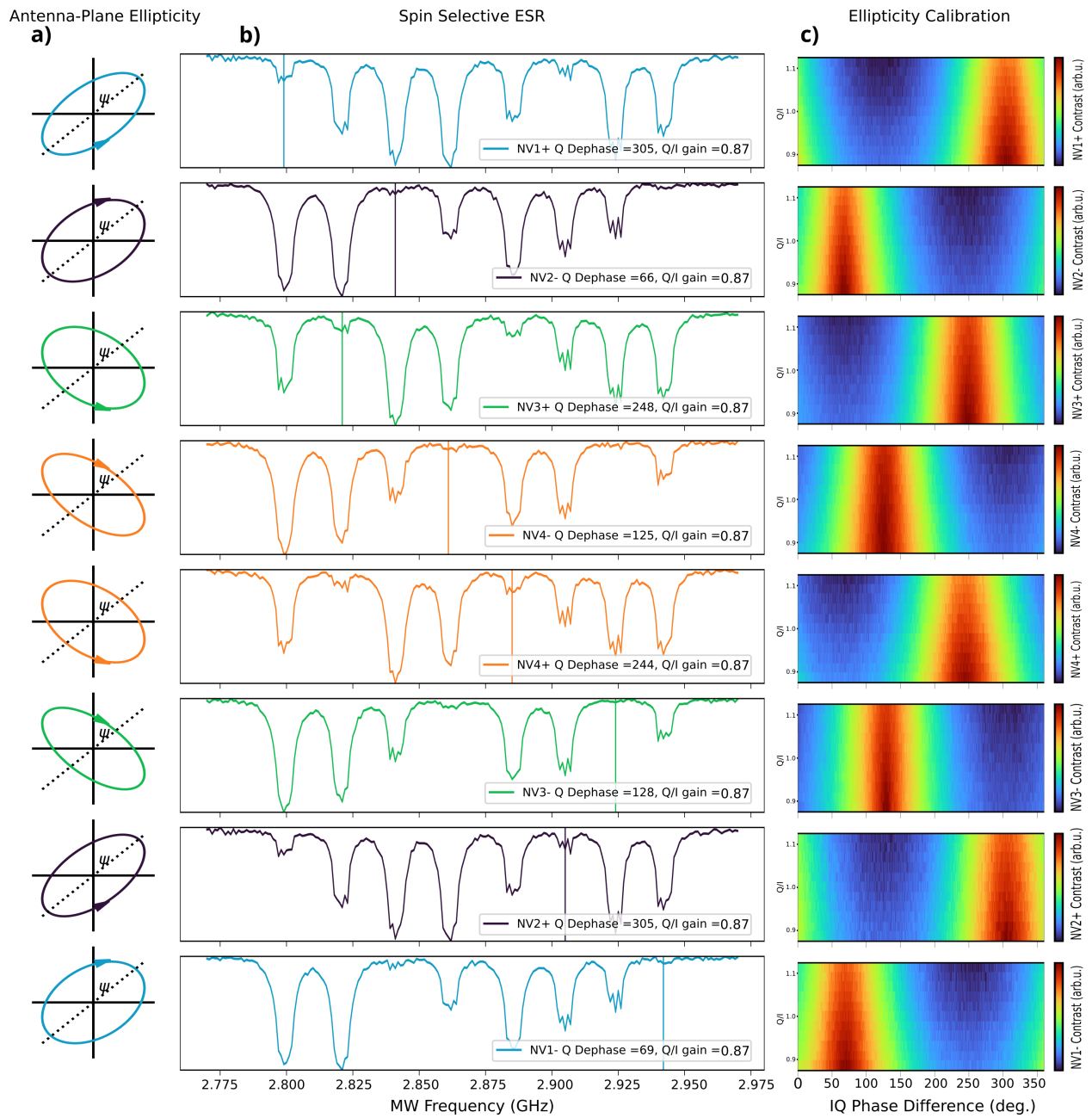


Figure S4: Results of the calibration using a confocal microscope and a flat diamond over the antenna. **a)** optimal spin-selective elliptic MW fields in the antenna plane. **b)** Record of the eight optimal MW field configurations to attenuate each peak in the ESR measurement. Because the diamond is almost flat on the antenna, peaks are attenuated by pairs. **c)** Calibration map to find the optimal attenuation of each transition line.

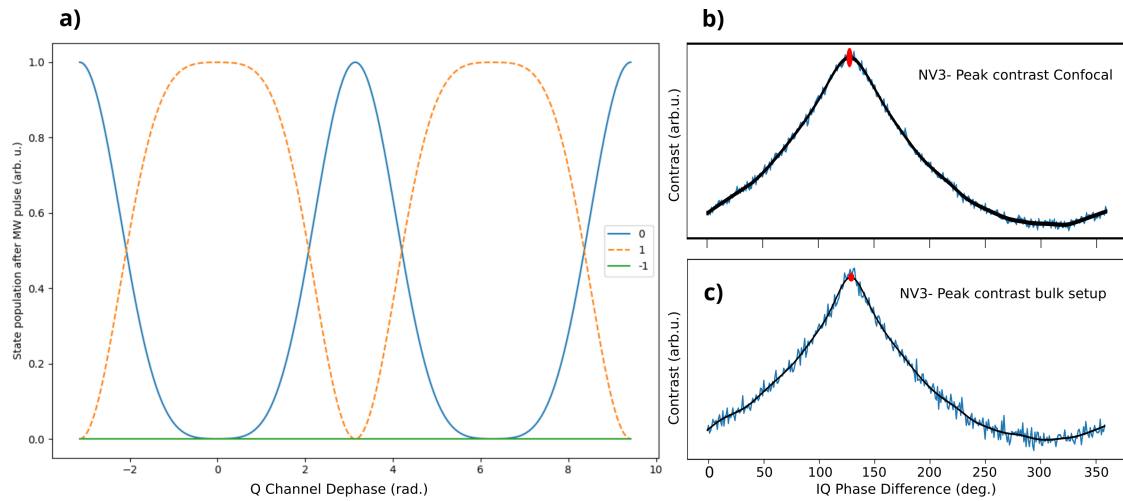


Figure S5: Theoretical and experimental phase dependence of peak attenuation. **a)** Simulation of the effect of phase in the population inversion attenuation of a π -pulse. **b)** **(c)**) Dependence of the peak attenuation on MW phase for the flat diamond confocal microscope (bulk tilted diamond) measurements. The black line represents the filtered signal using a Butterworth filter to find the optimal phase configuration over the signal noise.